



VERIFICATION OF THE SPATIAL AND
TIMING RESOLUTION OF THE SIEMENS
TOF-PET DETECTOR BASED ON THE
BIOGRAPH MCT FLOW

Tim Franssen

A research project submitted for the BSc of
Physics

First examiner: dr. P.G. Dendooven
Second examiner: dr. M. Kavatsyuk

May 7, 2018

Abstract

In vivo dose delivery verification is important in proton beam radiotherapy. It provides a way to verify and ensure that the protons deliver their dose to the desired location. One of the ways to verify the proton range is using in vivo positron emission tomography (PET). This report describes the specifications of a detector from the Siemens Biograph mCT Flow scanner in preparation for an investigation that will examine the capability of in vivo dose delivery verification using the short-lived positron emitter N-12. As a preparation, the detector's timing and spatial resolution was measured. This was done by using 2 scanner heads opposite to each other each consisting of 2 block detectors 43 cm apart, with a 8.1 MBq ^{68}Ge point source in between. The source was repositioned inside of the field-of-view in between measurements to examine the resulting effects. The temporal resolution was found to be 532 ± 5 ps and the spatial resolution to be 5.0 ± 0.1 mm. These are compatible with the values of 540 ps and 5.5 mm provided by Siemens.

1 Introduction

R. R. Wilson was first to suggest in 1946 the radiological use of high energy protons for medical use [23]. In 1958 the first patients were treated using proton therapy by C.A. Tobias et al[19]. From then on, research and treatment were performed on a small scale in research facilities for nuclear and particle physics. In 1990 the first hospital-based proton therapy center was opened at the Loma Linda University Medical Center in California. In the next 28 years techniques and devices have improved and as of April 2018 81 proton therapy centers are in operation. In 2018, our city Groningen opened its own facility: the GPTC (Groningen Protonen Therapie Centrum). On January 22th 2018, the first patients were treated there and the GPTC stated that it was a big success. The advantage of proton therapy over the main method used, photon therapy, is its smaller area of affected tissue. When a proton traverses through matter, it loses energy due to interaction. The energy loss can be described by the *linear stopping power* which is the energy lost per traversed path length. The stopping power has an inverse square relation with the speed of the photon, resulting in a high dose (energy deposited per kg tissue given in $J/kg = Gy$) delivery at the end of the proton's path. Often this phenomenon gets described by the protons *Bragg peak*, this being the peak at the end of the curve when the energy loss by ionization is plotted against the distance traveled through matter (the Bragg curve). Such a Bragg curve is shown in Figure 1 for protons and photons. The deposited dose by the protons ionizes and thereby harms the tissue. In treatment of a tumor it is the objective to 'destroy' the cancer cells by dose delivery. The localized high dose delivery is beneficial for the patient because surrounding healthy tissue will be less harmed. This is especially important when the tumor in question is located near vital organs. In photon beam radiotherapy, due to its broader energy deposition more healthy surrounding tissue is harmed.

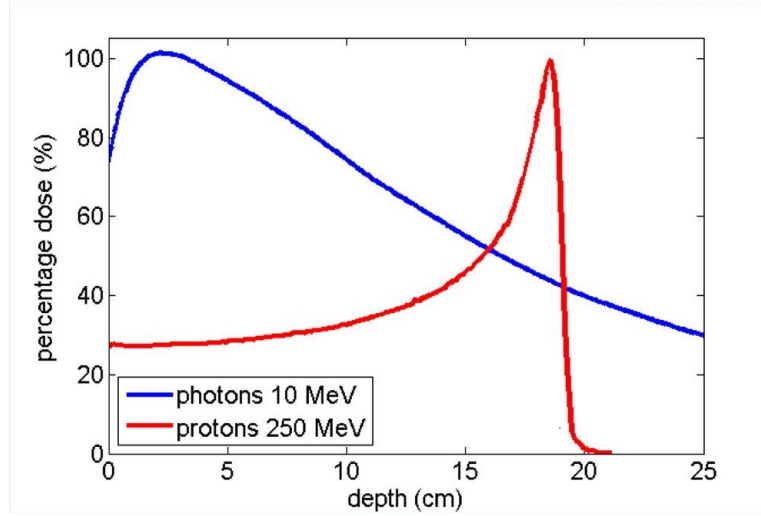


Figure 1: Dose vs Depth for photons and protons in water.[9]

Because a lot of dose is delivered in a tiny volume, it is important to make sure that the proton beam delivers its dose only in the right location. Proton therapy deals with some inaccuracies. How far in the body the high dose delivery will occur (proton depth) is dependent on the stopping power of the path it traverses. The stopping power differs for the material it travels through and thus one should know the composition of the tissue traveled through. This is done beforehand using a CT scan. The obtained proton depth is sensitive to changes. The treatment often takes between 25-40 days with daily irradiations. Changes in the patient's body (weight loss/gain) or different positioning can cause the proton depth to differ, resulting in an off-target irradiation. Also, the CT scan is performed with photons. Photons interact differently with matter than protons thus the stopping power for protons can't be found perfectly, resulting in an 3-4% inaccuracy in calculated proton depth.

Therefore, methods were developed to determine the proton depth *in vivo*. *In vivo* is Latin for in the living organism, meaning that the verification is done while the therapy is ongoing, not afterwards, such that it can be determined whether the beam is off-target. If that is the case, it can be corrected for before more healthy tissue is harmed. One of the prominent methods of verification is through positron emission tomography (PET) imaging. The supervisor of this bachelor project, dr. P.G. Dendooven, published in 2017 an article with his colleagues named 'Beam-on imaging of short-lived positron emitters during proton therapy'[2]. In this article, the capability of *in vivo* proton depth verification using short-lived positron emitters, of which ^{12}N dominates in human tissue, is proposed. In the future, this method of PET verification will be investigated further but instead of the Module TEK PET system from Philips Digital Photon Counting, a TOF-PET scanner based on the Siemens Biograph mCT will be used. Essentially, this report describes how the spatial and temporal resolution of the Siemens TOF-PET scanner is determined. To give this report context, information about PET imaging using short lived nuclei is added.

At the moment, there are two other promising methods of *in vivo* verification, *Prompt Gamma Imaging* and *Protoacoustics*. Articles on these topic are for instance 'Prompt-gamma monitoring in hadrontherapy: A review' by Krimmer et al [8] and 'Proton range verification in homogeneous materials through acoustic measurements' by Nie et al [10]. Going into detail in these methods is beyond the scope of this report, but a short explanation is given:

During the irradiation of tissue with a proton beam, prompt gamma rays are emitted on a sub-nanosecond timescale and are therefore very useful for in vivo verification. Smeets et al achieved in 2012, using a knife-edge slit prompt gamma camera "a range estimation of 1-2 mm (1σ) by irradiating a homogeneous PMMA target for number of protons that correspond to doses in water at the Bragg peak as low as 15 cGy at 100 MeV and 25 cGy at 160 MeV assuming pencil beams with a Gaussian profile of 5 mm sigma at target entrance"[18]. In 2016, the first clinical application was realized by Richter et al[14], using a prototype of a knife edge slit camera being developed by IBA (the same as Smeets et al). They conducted their measurements during the treatment for head and neck tumors and measured range variations of ± 2 mm.

Protoacoustics is yet less developed than the other two methods but already very promising results were achieved. When a proton deposits its dose, an acoustic pressure wave is generated due to the increase in temperature following the dose deposition. The frequency, amplitude and shape of the wave depend on the dose delivered and material. These can be found using a hydrophone behind the phantom in the proton beam propagation axis. Using the time difference measured between the prompt gamma rays and the acoustic waves the proton depth is estimated. Assman et al [1] achieved in 2015 a reproducibility of range measurements of $\pm 30 \mu\text{m}$ in a water phantom. Nie et al[7] published in 2018 a simulation study for the liver and prostate case to investigate the usefulness in non-homogeneous material. For the liver case they achieved a range verification of 0.4 mm and for the prostate case ≤ 1.6 mm.

2 In-beam PET for in-vivo dose delivery verification.

2.1 Positron Annihilation Tomography

During the irradiation, positron emitting nuclides are created in the tissue. The atoms most abundant (in number) in the human body are in order: ^1H (62%), ^{16}O (24%), ^{12}C (12%), ^{14}N (1.1%), ^{40}Ca (0.22%), ^{31}P (0.22%)[22]. Except for ^1H , positron emitters are created from these during irradiation, namely: ^{10}C , ^{11}C , ^{12}N , ^{14}O , ^{15}O , ^{29}P , ^{30}P , ^{38g}K and ^{38m}K . ^{38g}K and ^{38m}K being respectively the ground state and the excited state of Potassium. These nuclides decay by emitting a β^+ particle. This emitted β^+ particle makes its way through the matter losing its energy by interaction with nuclei and electrons until it finally annihilates with an electron. As a result, two 511 keV photons are emitted at 180 degrees relative to each other. PET imaging uses this mechanic by capturing both of the photons on each side and constructing the straight line along which they originated, the line of response (LOR). This is most commonly done in the clinical environment by a ring of PET detectors connected to each other surrounding the tissue of interest. When two detectors measure a 'hit' in a certain time interval (the *timing window*), it will be registered as a coincidence and the two crystal id's (signifying the location on the detector) are used to make the LOR. A further explanation of the structure and operation of the PET detector is given in section 2.2. From the collection of LOR's, a full picture is made with more counts meaning more activity from that area. A more precise way of PET is the Time Of Flight PET (TOF-PET). This method uses the same way of reconstructing the line of response but incorporates the time difference between the hits in the two crystals. With the time difference, the probability of where on the line of response the positron annihilation actually happened is known. Figure 2 illustrates the advantage of TOF-PET over PET.

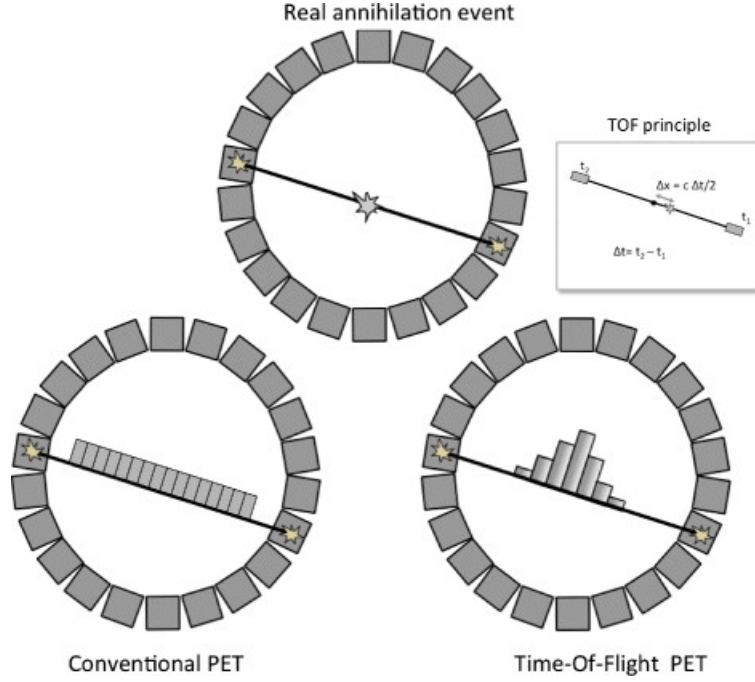


Figure 2: Conventional PET and TOF-PET[20]. In conventional PET the source of the positron annihilation is measured to have the probability to be anywhere on the line of response, with TOF-PET this area is shortened.

2.2 The PET scanner

The concept of a PET detector is fairly straightforward. A PET scanner is made up by a grid of scintillation elements (crystals) connected to photomultiplier tubes. The purpose of the scintillation crystals is to detect incoming 511 keV photons and convert their energy to visible light. Suitable scintillation material absorbs the 511 keV photons and afterwards emits more photons of its own. Important characteristics of commonly used scintillation materials are given in table 1. PMT's convert the visible photons from the scintillation crystals into a current that can be measured. Early PET scanners consisted of multiple scintillation crystal connected to their own photomultiplier tube. In order to improve the spatial resolution, the scintillation crystals became smaller and therefore more were needed per detector to cover the same area. It turned out to be too expensive to also minimize the PMT's and so in 1980 the block detector was designed by Casey and Nutt. In a block detector four PMT's are used, each covering one quarter of an array of small scintillation crystals. The exact position of the scintillation crystal hit can be calculated by equations 1 and 2.

$$X = \frac{(PMT_A + PMT_B) - (PMT_C + PMT_D)}{PMT_A + PMT_B + PMT_C + PMT_D} \quad (1)$$

$$Y = \frac{(PMT_A + PMT_C) - (PMT_B + PMT_D)}{PMT_A + PMT_B + PMT_C + PMT_D} \quad (2)$$

Where X is the x-position and Y the y-position of the crystal hit and $PMT_{A,B,C,D}$ the output of each respective PMT (A, B, C or D).

Table 1: Available scintillation materials [16]

Property	Characteristic	Desired value	LSO	BGO	GSO	NaI
Density (g/cc)	Defines detection efficiency of detector	High	7.4	7.1	6.7	3.7
Effective atomic number	Scanner sensitivity	High	65	75	59	51
Decay time (ns)	Defines detector dead time and randoms rejection	Low	40	300	60	230
Relative light output (%)	Impacts spatial and energy resolution	High	75	15	35	100
Energy resolution (%)	Influences scatter rejection	Low	10.0	10.1	9.5	7.8

When considering efficiency of the detector one should consider the density and effective atomic number of the scintillation material. Both of these characteristics improve the attenuation. The higher these two values, the higher the probability that a photon will be absorbed when traveling through.

Decay time is an important factor for in vivo application. With a shorter decay time of the scintillation mechanism the timing resolution of the system increases.

The relative light output is the yield of scintillation photons per keV of energy the scintillation crystal has absorbed. When this yield is higher, the energy resolution is better. When considering the rejection of scattered photons (section 2.3) with less energy, a better energy resolution is useful.

Some scintillation material fits a certain purpose better than the other. For instance if your research puts an emphasis on measuring gamma-ray energies NaI is most suitable. But if you're dealing with a high count rate LSO is optimal due to its small decay time.

After being ejected by the scintillation crystals, the *scintillation photons* are entering the four PMT's. The purpose of these PMT's is to amplify the light for better measurements and convert it to a measurable current. An illustration of the inside and how it operates is given in Figure 3. The inner surface of the entrance window of a PMT is coated with a photo-emissive material, the photocathode. Whenever visible light lands on the photocathode it has a probability of ejecting an (photo-)electron, this probability is referred to as its quantum efficiency and is typically around 25-35% for a PET scanner. Behind the photo-emissive material, there are several dynodes (often ranging from 9 to 12). The photoelectrons get directed towards the first dynode by a focusing grid. The dynode is coated with a material that has high secondary emission characteristics. When a high speed electron hits a dynode, the dynode's surface ejects several secondary electrons of its own. The electron multiplication factor depends on the energy of the photoelectron, which in turn is determined by the voltage difference between the dynode and the photocathode (or the dynode and the previous dynode). Secondary electrons are led to the next dynode which has a higher voltage and the same process occurs. This multiplication step happens depending on how many dynodes are built into the PMT. After the last dynode the electrons are collected by the anode. This current can be measured and is proportional to the light signal received.

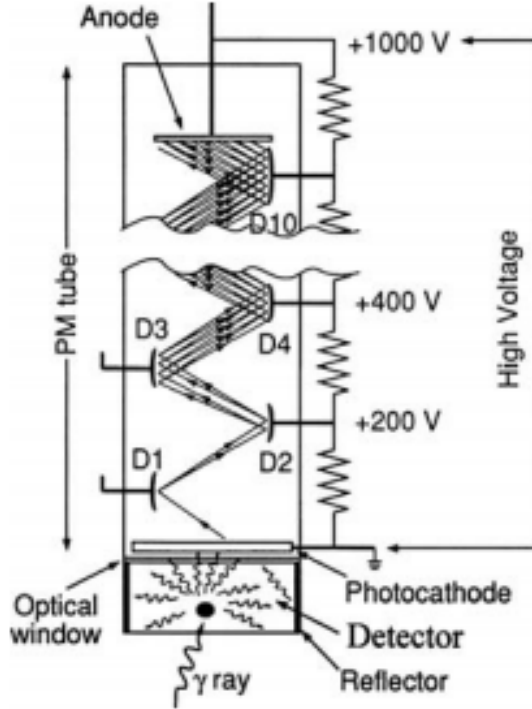


Figure 3: The inside of a PMT[6].

2.3 Accuracy in positron emission tomography

Positron emission tomography is a good method of imaging, but there are still a few factors limiting its accuracy. Some of these are related to the scanner technology and could be optimized in the future. But some are due to principles in nature and can only be accounted for in the statistics.

Let's start with the physical process of positron emission itself. When the positron emitters are created they don't decay immediately. When considering long-lived nuclides, a problem that is faced is biological washout. The body is always circulating inside and nuclides get transported throughout the body. When considering those long-lived nuclides it happens that a radioactive nuclide is transported over a large distance before it decays such that it gives a wrong location and thus misleading data. Since this research is performed in the context of imaging of very short-lived nuclei ($\tau_{\frac{1}{2}} = 11.0$ ms), this effect can be neglected.

When the nuclide eventually decays, the positron gets emitted with a certain kinetic energy and makes its way through the tissue. Every time it interacts with an electron or a nucleus it gets scattered and loses a bit of its kinetic energy. Due to this scattering, the positron travels in an unpredictable tortuous path. Eventually, when most of its kinetic energy is lost, it annihilates with an electron. The length of the path that is taken varies radically, depending on its initial kinetic energy and how it scattered, and is impossible to predict. In reports like that of *J. Cal-González et al* [3], the mean proton range in different tissue is estimated. Oftentimes nuclides with shorter decay times have higher initial positron energy and therefore a longer mean positron path. ^{12}N has a relative high initial maximum positron energy of 16316 keV [11]. In the article by *Dendooven et al (2015)*[5], the root-mean-square of 1-dimensional positron range of ^{12}N was

estimated to be 18 mm in water. This positron travel range is certainly a problem when applied to the human body due to its inhomogeneity resulting in different lengths of the path in different directions. Before annihilation, the positron and electron have momentum in a certain direction because of the thermal energy. This momentum causes the photon pair to deviate from the perfect 180 degrees. This effect is called *non-collinearity* and when an distribution of angular spread is made the full width at Half Maximum (FWHM) is equal to 0.50 degrees Resulting in a spread of 180 ± 0.25 degrees.

There are three types of measured coincidences that can be classified. True coincidences, scattered coincidences and random coincidences. True coincidences are desired since they give the right LOR. A positron annihilates with an electron and both of their photons go their straight way to a scanner without any interaction with the matter they pass through. The two possible alterations that will still be considered by the scanner as a true count are shown in figure 4.

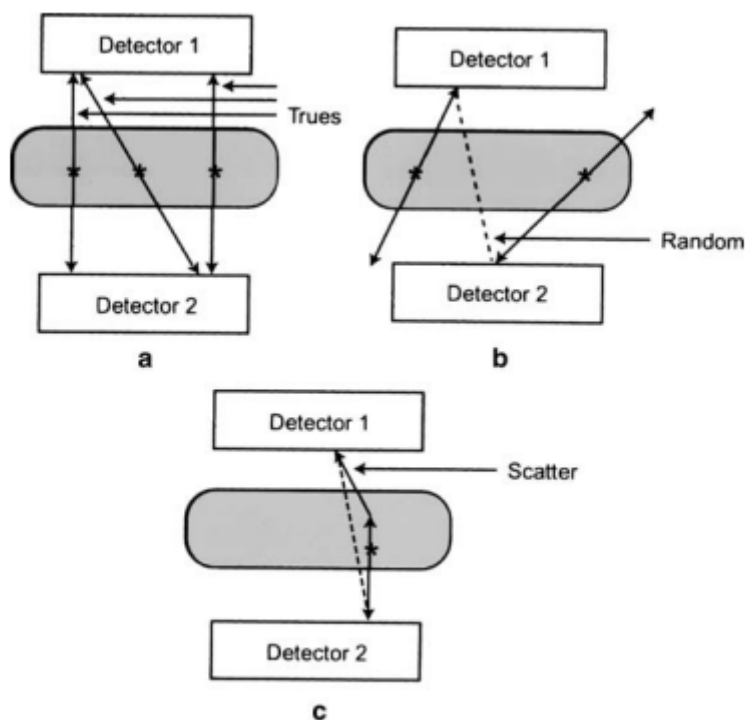


Figure 4: a) true coincidences, b) random coincidence caused by two separate events, c) a scattered coincidence caused by interacting with matter[6]. The gray area in the middle represent the object that is being imaged, the stars represents positron annihilations and the arrows the path the 511 keV photons traveled.

It is possible that two different annihilations happen inside the material and of each event only one photon gets registered by a detector. If these two are registered in the same timing window, they will be registered as a true coincidence. It can also happen for instance that four photons get registered at the same time and the wrong pairing of each event is made. These incorrect events give a wrong line of response that blurs the image. The number of random coincidences that is estimated to occur is related to the count rate in each of the detectors (N_A and N_B) and the timing window τ in the following way:

$$R_{rand} = N_A N_B \tau \quad (3)$$

The rate of random coincidences is linear with the timing window and the count rate in each of the detectors. This time window can be made shorter/longer in the software of the scanner but is also influenced by the scintillation material used by their decay time.

The other kind of coincidence that gives a wrong line of response is the scattered coincidence. In this case, at least one of the photons has had an interaction with an electron by Compton scattering. When a photon is Compton scattered, it transfers part of its energy to a loosely bound electron. Due to the exchange, the electron is ejected from its orbit and the photon loses some of its energy and changes its direction. The relation between energy loss and scatter angle is given by the Compton equation[12]:

$$E'_\gamma = \frac{E_\gamma}{1 + \frac{E_\gamma}{m_0 c^2} (1 - \cos(\Theta_c))} \quad (4)$$

where E'_γ is the energy after scattering, E_γ the original energy, m_0 the mass of an electron and Θ_c the Compton angle. For example, a 511 keV photon interacts with an electron and is scattered over 30 degrees. Formula 4 tells us the photon has 451 keV left and will by most PET scanners still be counted as an event. The energy window is typically between 435-650 keV[12]. During proton therapy, 511 keV photons have to travel through dense tissue, Compton scattering will occur more often than in the case where measurements with a source in air are discussed. A photon has a higher chance of Compton scattering when traveling more distance through a material and when travelling through a denser material.

It can also be the case that the photon is Compton scattered away from the detector and won't even reach it. This case combined with the 'absorption' of the photon in the object by *the photoelectric effect* is defined as the attenuation. Attenuation should be corrected for since photons traveling more distance through tissue or through tissue with a higher density have less probability to reach the detectors. Without a correction it can seem like a dip in counts at a position from which the photons have to travel through more or denser matter. A good illustration is given in Figure 5. [25] .

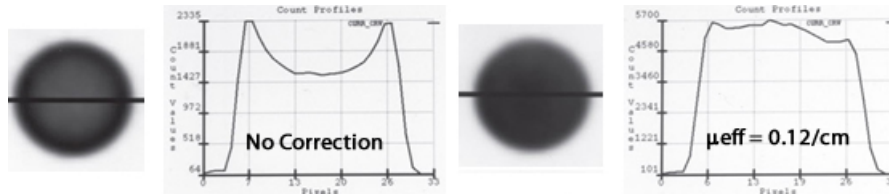


Figure 5: A PET scan of a radioactive circle phantom inside a spherical object. The photons from the middle have to travel more distance through the attenuating material (than those from the edge) and are thus more likely to be attenuated. A correction factor increasing from the edges to the middle is used to account for the attenuation.

The probability for attenuation is:

$$P = 1 - e^{-D\mu_l} \quad (5)$$

Where D is the thickness of the material and μ_l is the linear attenuation coefficient of the material. When working with human tissue, this expression becomes complicated since every

part in the body has its own attenuation coefficient. So equation (5) can be written as

$$P = 1 - e^{\sum D_i \mu_i} \quad (6)$$

The index i refers to the tissues along a certain path. Some μ_l values of useful materials for 511 keV photons are given in Table 2[12].

Table 2: Narrow-beam (scatter-free) linear attenuation coefficients for a 511 keV photon.

	μ_l (cm ⁻¹)
Adipose tissue	0.090
Water	0.095
Lung	≈ 0.025 -0.004
Smooth muscle	0.101
Cortical bone	0.178
LSO	0.866
BGO	0.95

Dead time is a property of the scanner itself that decreases the measured count rate. A PET scanner can be viewed as a series of subsystems, each of them requiring a certain amount of time to finish its process. For instance, when a photon hits a certain crystal, the crystal has to decay, the photons from the crystal have to travel through the PMT's which at the end cause a pulse to be generated. This pulse gets amplified and the energy and spatial position is evaluated and finally the count is recorded. During this time the detector can't register another count. The dead time is dependent on the time needed for each of these consecutive processes. When regarding dead time there are two types of systems: paralyzable and nonparalyzable. In paralyzable systems, each event introduces a dead time even if it's not counted. Consequently, while in the dead time of one event, another event will prolong this. Nonparalyzable systems ignore any events during the dead time of the previous, with no effect on subsequent events. A paralyzable system will eventually saturate if the count rate gets to a certain level and decrease in counts measured while the actual counts per area increases. Formulas for count rates in the paralyzable case (equation 7) and the nonparalyzable case (equation 8) are given below. m is the measured count rate, n the actual one if everything would be recorded and τ the dead time from a single event.

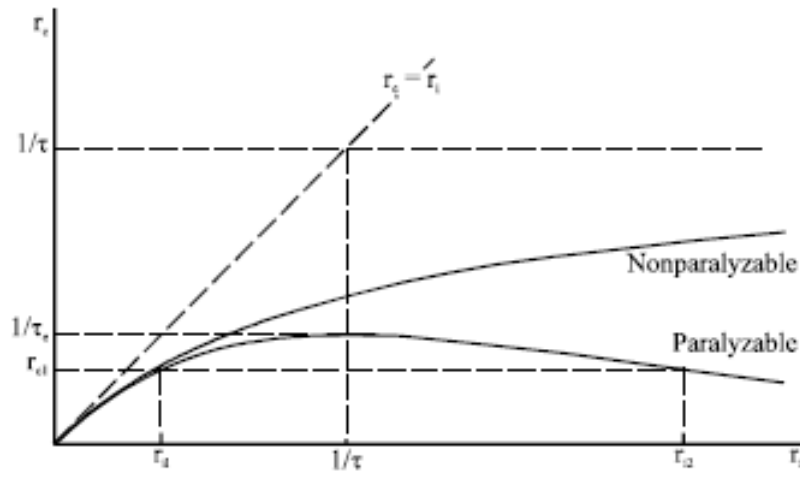


Figure 6: Registered Count rate vs actual count rate for a paralyzable and non-paralyzable system[15].

$$m = ne^{-n\tau} \quad (7)$$

$$m = \frac{n}{1 - n\tau} \quad (8)$$

If a photon enters a crystal at an angle, there is a probability that it passes through without interacting to an adjacent crystal and gets absorbed by that crystal. This results in an error in the constructed LOR and is named the parallax effect. In the measurements of this report this effect is small due to the positioning of the point source and the scanner. The scanner panels are 10.16 cm (4 inches) in width and the distance between a source and the scanner is 21.5 cm. The angle at the edge of the detector would be up to $\tan^{-1}(\frac{5.08}{21.5}) \approx 4.2^\circ$.

2.4 N-12 imaging

As mentioned before in the introduction, this report is a preparation (by measuring the resolutions of the Siemens detector) for an investigation examining the verification of the range of a proton beam using primarily ^{12}N TOF-PET imaging. Two interesting articles on the subject are 'Short-lived positron emitters in beam-on PET imaging during proton therapy' (*Dendooven et al 2015*) and 'Beam-on imaging of short-lived positron emitters during proton therapy' (*Buitenhuis et al 2016*)[2].

To give a short indication on the content of those reports, Dendooven et al (2015) went over the short-lived positron emitters that get created during proton irradiation. They were interested in in vivo verification so they defined *short-lived nuclides* as nuclides with a half-life shorter than that of ^{10}C ($T_{1/2} = 19.3$ ms) and measured their production in the stopping of 55 MeV protons in water, carbon, phosphorus and calcium. The production rates found were used to calculate the production rates in tissue. They found that for carbon-rich adipose tissue ^{12}N dominates the PET count rate up to 70s after the start of an irradiation. On bone tissue ^{12}N dominates over ^{15}O during the first 8-15 seconds, depending on the carbon-to-oxygen ratio.

In *Buitenhuis et al (2016)*, in vivo beam-on imaging of the proton range using these short-lived nuclides was performed. A measurement was conducted in which the coincidences were

Table 3: Important properties of the Siemens Biograph mCT Flow PET scanner

PET Detector Assembly		
Detector material	LSO	
Detector element dimension	4x4x20 mm	
Detector elements per block	169	
Photomultiplier tubes (PMTs)	4 per block	
PET Data Acquisition/Processing		
Coincidence window	4.1 nsec	
System energy resolution	≤12% FWHM	
System time resolution	540 psec typical	
Acquisition modes	FlowMotion, static multi-bed, listmode	
PET NEMA 2007 Spatial Resolution – Axial (Typical)	Standard Processing (256x256)	HI-REZ Processing (400x400)
FWHM @ 1 cm (mm)	5.5	4.5
FWHM @ 10 cm (mm)	6.0	5.9

measured while the beam was on. To subtract the long-lived background counts, a method was developed using a beam-off period in-between. This resulted in a 30 ms beam-on period alternating with a 59 ms beam-off period. They measured a 5 mm range shift as 6 ± 3 mm using the N-12 profile. A simulation has shown that with a large dual panel scanner that images a spot exactly after it has been delivered can achieve an accuracy of 5.5 ± 1.1 mm for a 5 mm range shift for 1×10^8 protons. For a beam of 5×10^8 protons this becomes 5.2 ± 0.5 mm.

Coincidences originated from ^{12}N are measured the most when verified during or immediately after irradiation in human tissue. That’s why the emphasis is mainly on ^{12}N . Because of its short half-life, very quick feedback is given, and it negates biological washout. A slight disadvantage is the high energy of the positron emitted as mentioned previously in section 3.3. Still *Buitenhuis et al (2016)* achieved a good accuracy. Important in in vivo verification is the immediate detection of bigger errors. The smaller errors could afterwards be found with the more precise data from long-lived nuclei.

3 Instruments and methods

3.1 Siemens PET scanner

In the measurements the Siemens detectors from the Biograph mCT Flow are used. The specifications important for this report are given in Table 3 and the full specifications can be found in the product specification sheet[16]. The intention of the Biograph mCT Flow is to be applied in a medical setting. Fully, it consist out of 3 rings of each 48 block detectors. In total this equals to 24336 detector elements. In this experiment we only aim to find the spatial and temporal resolution so only 4 detectors are used, in pairs of two on each side.

3.2 Experimental set up

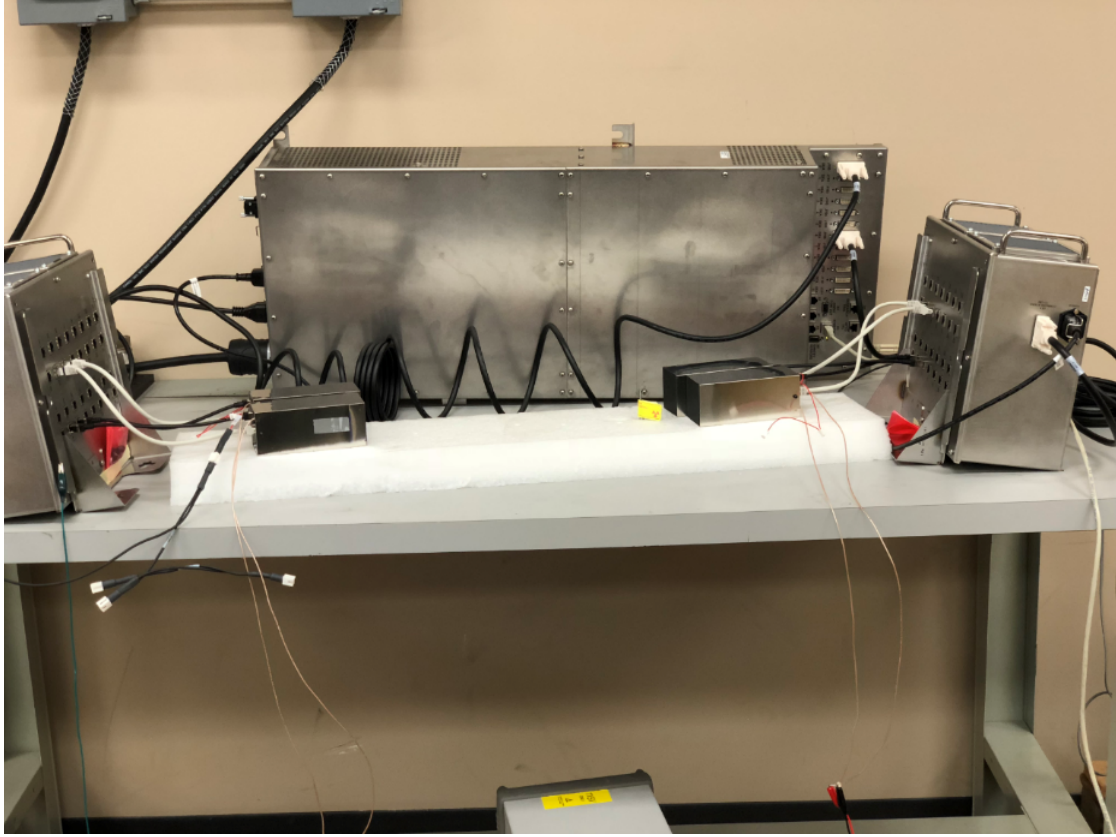


Figure 7: Experimental set-up. On each side two scanner panels consisting of two detectors blocks can be seen. Scanner panel A on the right and B on the left. The block detectors are connected to a device (DEA) that analyses the signal and converts it to digital data. One scanner panel can consist of 4 by 4 block detectors, thus the 16 inputs in the analyzing device. The DEA sends the digital data to the large *coincidence-unit* in the back. The coincidence unit considers hits from both scanner panels, pairs the valid coincidences and sends them to the computer.

The measurements were meant to be performed in the KVI-Center for Advanced Radiation Technology (KVI-CART) in Groningen. Due to the unavailability of the detectors and a deadline which had to be kept, the measurement data was taken elsewhere. The measurements were conducted at Siemens Molecular Imaging in Knoxville by M. Kapusta. A picture of the set-up is shown in Figure 7. Five measurements were performed in total with the same distance and orientation of the detectors. The difference between the measurements is the placement of the source in between. The location of the source per measurement is given in Figure 8. In the first measurement, the source is located exactly in the middle, 21.5 cm from each detector side. In the second measurement the source is relocated 3 inches (7.62 cm) towards scanner panel A, in the third 3 inches towards scanner panel B. In the fourth measurement, the source is located in the same distance to both scanners as the first measurement but moved 2 inches to the right,

in the fifth, 2 inches to the left. It should be noted that because we could not perform these measurements ourselves we're not sure about the accuracy of given values. From some of the data that has been processed slight inaccuracies were found. This isn't a problem but it is possible that with some improvements in positioning better resolution can be found. All measurement were performed with an acquisition time of 10 min and a ^{68}Ge point source of 8.1×10^6 Bq.

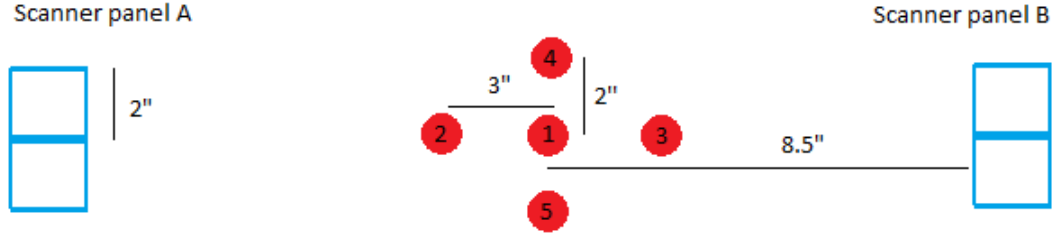


Figure 8: Position of the source in the 5 measurements. Distance is given in inches.

3.3 Data reconstruction methods

If a coincidence is registered in the hardware to which the scanners are connected, it is stored in an 8-byte 'word' containing information about the crystal ID number of each scanner side and the time difference. The crystal ID is a value ranging from 1-2704 (52x52) signifying the location of the crystal on the scanner head. 52 because a complete scanner head consists out of 4 by 4 block detectors each containing 13 x 13 crystals. The crystal ID is counted upwards in the y-direction and in the x direction with steps of 52. It means that for instance Crystal ID 35 has a crystal location of (x=1 , y=35) and 89 a crystal location of (x=2 , y=37).

The raw data comes out after the measurement as a .l64 file. MSc I.S. Ozoemelum provided us with a C++ program which decodes these event 'words' into useful data. This datafile consist of a string of values, each 8 consecutive ones regarding 1 coincidence event. These 8 values contain the above mentioned crystal ID's of both scanner head and their deconstructed coordinates, the time difference and whether it was considered a valid coincidence (since it only registered valid coincidences it was always 1).

MATlab was used in order to reconstruct an image from the data. Important to note is that one should verify whether the block detectors are connected to the desired input of the analyzing device (DEA). As mentioned the DEA has 16 inputs for block detectors, with each their own 13 by 13 crystals (Figure 9). Reconstruction makes use of this order, so it is important that if in reality the detectors are next to each other, it also shows in the reconstruction. If everything is connected properly, this shouldn't be a problem. But if it isn't, it can be corrected for in the data by adding/subtracting to the crystal ID.

With our algorithm, MATlab goes over every coincidence and creates its LOR. Using the approximate distance of the source to the scanners, the reconstruction plane is established and it collects all the intersections of that plane with the LOR's. The reconstruction plane is a plane equal to and parallel to the surface of the scanner panels located at the position of the source. The resulting image is a flood map showing the number of intersections with a LOR per location on this reconstruction plane. This can be used to measure the spatial resolution of the scanner, by constructing the 1D distribution of coincidences per unit length and fitting a Gaussian. Since

the source can be considered a point source, the FWHM of this fitted Gaussian is equal to the spatial resolution of the detector.

Another MATLAB program collects the time difference for every coincidence in a crystal. The time difference being the time between a registered hit in scanner panel A and the matching hit in scanner B plus some constant C. This constant is added in reconstruction, but since every measurement has the same constant added and of importance is only the difference in time (between measurements or to calculate the FWHM), this constant doesn't influence the outcome. The distribution of time difference is stored in 64 bins of 78 ps. To retrieve the timing resolution of a crystal, a counts vs time difference distribution is made and a Gaussian is fitted. The FWHM is the timing resolution for that crystal.

The Gaussian that will be fitted throughout this report are of the form:

$$y = a * e^{(\frac{x-b}{c})^2} \quad (9)$$

b is an estimation of the x-position of the peak and c can be used to obtain the FWHM by the relation:

$$FWHM = 2\sqrt{\ln(2)} * c \quad (10)$$

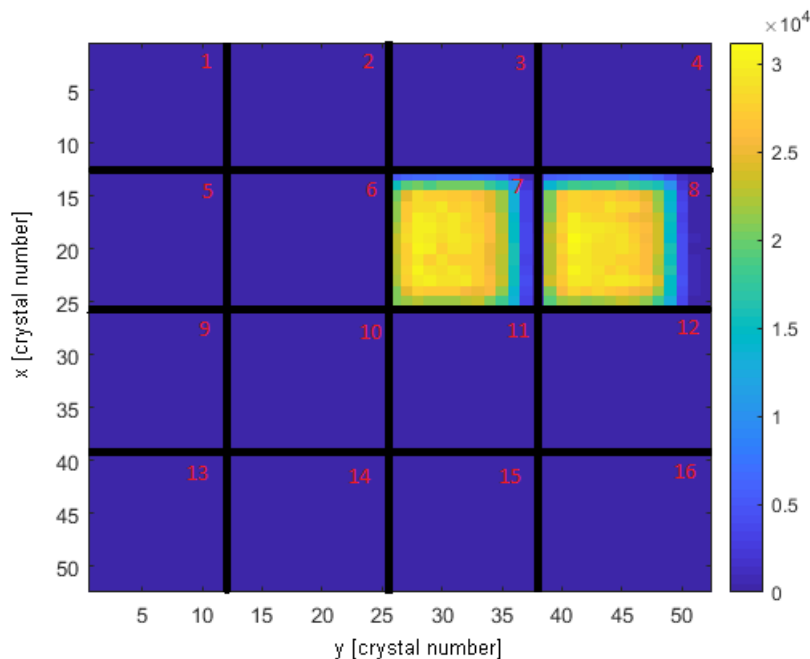


Figure 9: A full reconstruction consists of 16 block detectors. For reconstruction it would be essential, considering the set-up of Figure 7, that the block detector in field 8 would be moved to 11 (or better yet, 7 to 5 and 8 to 9).

4 Results

The five measurements were performed at Siemens Molecular Imaging in Knoxville by M. Kapusta on March 28th. In each individual measurement a ^{68}Ge source with an activity of $8.1 * 10^6$ Bq

was used with an acquisition time of 10 minutes. In between measurements, the source changed position as indicated in Figure 8.

4.1 Timing resolution

As described in section 3.3, the time difference of every coincidence is stored and a distribution for every crystal is created. Figure 10 shows the time difference distribution for crystal 979 in the first measurement. Crystal 979 is located in the middle of the right (when viewed from the source) block detector in scanner panel A and is chosen for its high count rate in the first three measurements. In the fourth measurement, a crystal near the right edge is chosen with crystal ID 760 and in the fifth measurements, a crystal at the left edge of the scanner panel with crystal ID 1342, also for the reason of relative high count rates. Figure 10 gives a timing resolution of 566 ± 6 ps. In the second and third measurement the source is placed closer to one of the two detectors and that is easily noted from their time difference distributions in Figure 11. Notable is the increase in counts and the displacement of the position of the peak. As the source is moved towards scanner panel A, the time difference measured will go up, as it is moved closer to scanner panel B, it will go down. From the difference in peak-position, with the speed of light, the exact displacement of the source can be found. Between the first and second experiment, the peak is shifted with 502 ± 4 ps which corresponds to a distance of 7.5 ± 0.1 cm. The peak is shifted -544 ± 4 ps between the first and third measurement resulting in a displacement of -8.2 ± 0.1 cm. These results will prove useful in finding the spatial resolutions.

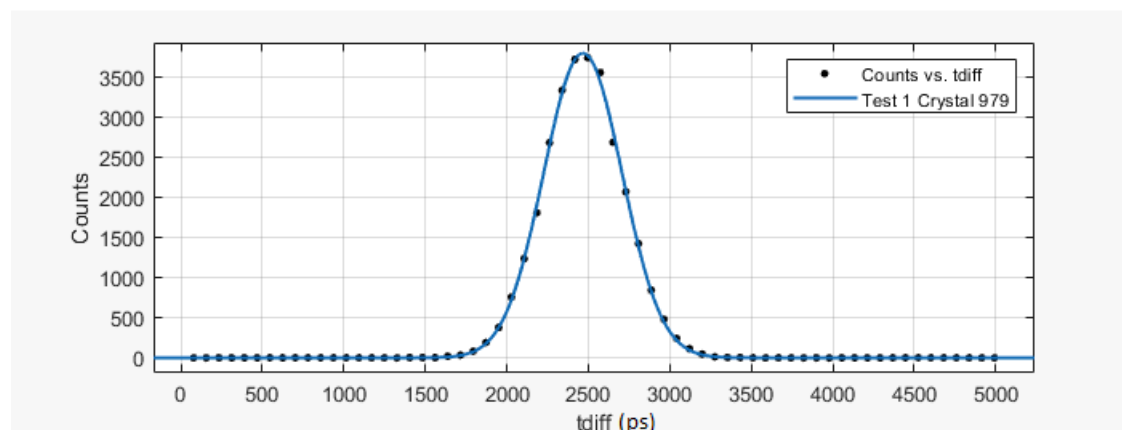


Figure 10: Measurement 1 Crystal 979: Gaussian fitted time distribution with parameters:
 $a = 3801 \pm 30, b = 2467 \pm 3, c = 340.1 \pm 3.1$ and a R^2 of 0.9992.

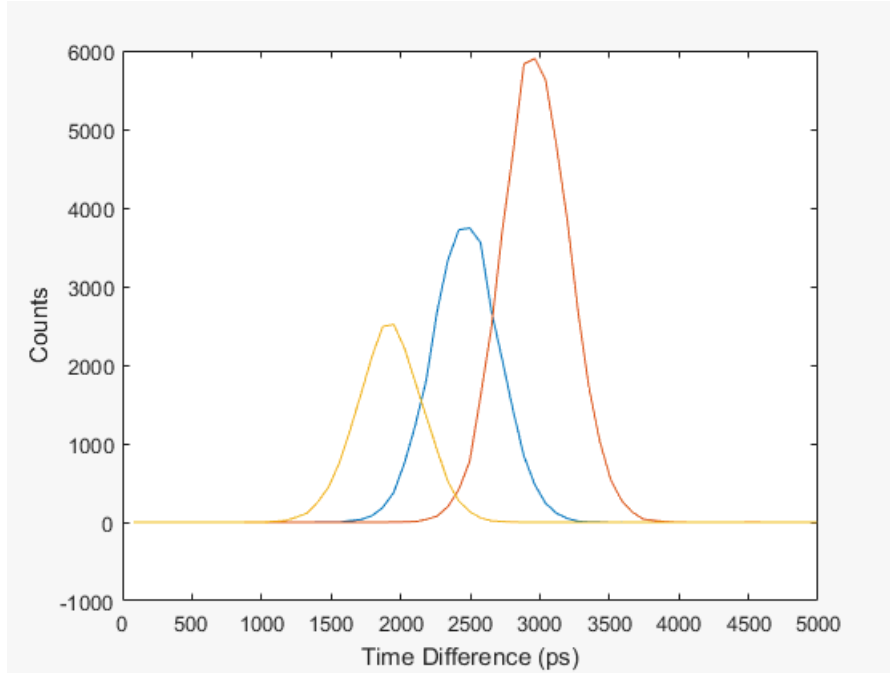


Figure 11: Time difference distribution in crystal 979 for measurement 1 (middle), 2 (right) and 3 (left).

In every measurement, the timing resolution was gathered for a crystal with a relative high count rate. These results are given in table 4. Also, the timing resolution of a whole row of crystals of one block detector at a fixed height was measured to examine whether the position of a crystal inside the block detector has influence on its timing resolution. These can be found in table 5.

Table 4: Timing resolution.

Measurement	Crystal ID	Timing resolution (ps)	Position peak of the Gaussian (ps)	Averaged count rate on crystal (cps)
1	760	517 ± 6	2563 ± 2	33.6
1	979	566 ± 6	2467 ± 3	49.1
1	1342	518 ± 5	2565 ± 2	37.1
2	979	570 ± 5	2969 ± 2	77.3
3	979	554 ± 5	1923 ± 2	31.4
4	760	536 ± 8	2759 ± 4	44.2
5	1342	506 ± 5	2423 ± 2	11.4

4.2 Spatial resolution

The reconstruction of the midplane image was done as described in section 3.3. To check whether the positioning of the scanners is correct a flood map of both scanner panels is made, these can be seen in Figure 12 and 13 for the first measurement. The flood map represents the intensity of

Table 5: Measurement 1: Timing resolution for 13 adjacent crystal at fixed height.

Crystal ID	x-position (mm)	Timing Resolution (ps)	Averaged Count Rate (cps)
708	2	526.8	2.0
760	6	517.6	33.6
812	10	530.4	44.7
864	14	528.4	46.2
916	18	546.5	49.3
968	22	557.6	49.0
1020	26	560.5	49.3
1072	30	560.5	48.6
1124	34	538.6	46.1
1176	38	516.4	48.0
1228	42	518.5	48.6
1280	46	507.5	46.0
1332	50	514.8	36.3

coincidence counts for every crystal in the detectors. The reconstruction algorithms were used to reconstruct the midplane images. The midplane image of the first measurement is given in figure 14.

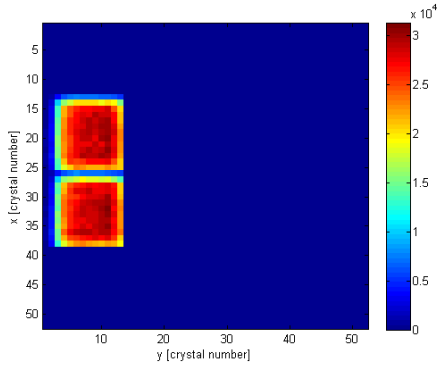


Figure 12: Measurement 1: Flood Map Scanner Side A.

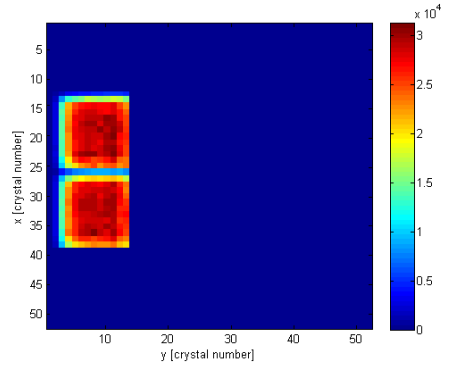


Figure 13: Measurement 1: Flood Map scanner side B.

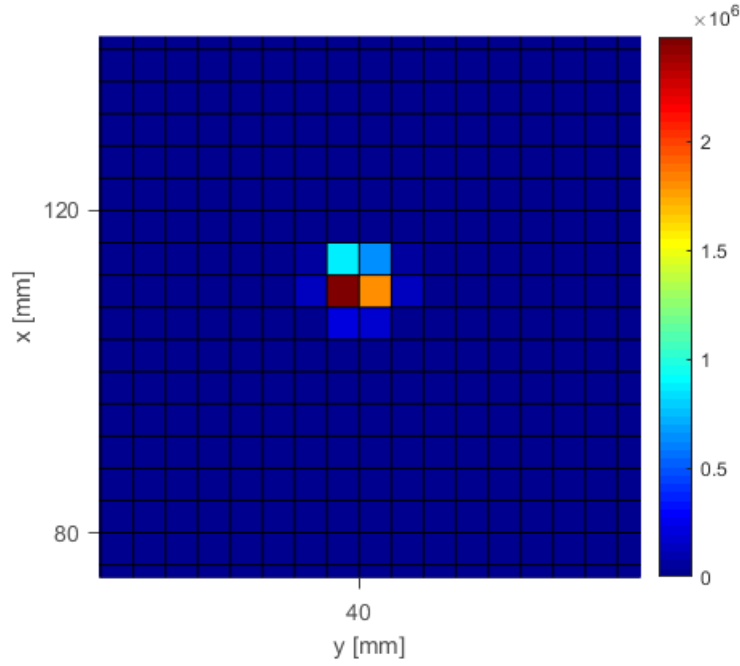


Figure 14: Measurement 1: Reconstructed midplane image.

To examine the spatial resolution of the detector, the amount of coincidences at the height of the source was set apart to create a 1D-distribution. A Gaussian was fitted in this spatial distribution and can be seen in Figure 15. The Gaussian in Figure 15 gave a spatial resolution of 5.0 ± 0.1 mm.

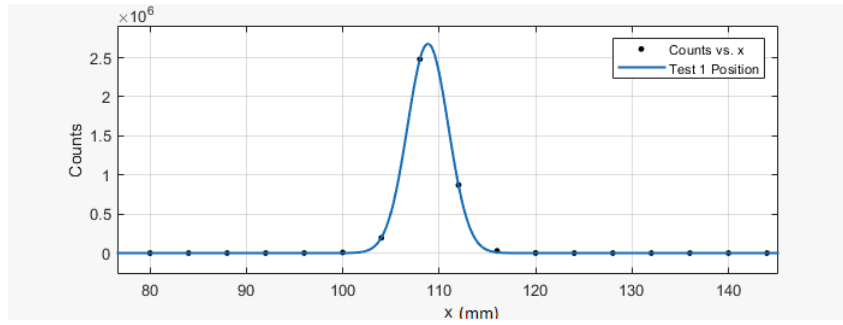


Figure 15: Measurement 1: Gaussian fitted Position distribution with parameters: $a = (2.68 \pm 0.01) * 10^6$, $b = 106.8$, $c = 2.99 \pm 0.02$ and a R^2 of 0.9999.

For the second and third measurement, another method of reconstruction had to be used since the source wasn't located in the midplane. Thus the plane of reconstruction had to be moved to the position of the source to obtain the sharpest possible image. In section 4.1 was

found, that the source was moved approximately 7.5 ± 0.1 cm towards scanner panel A in the second measurement and 8.2 ± 0.1 cm towards scanner panel B in the third measurement. From that approximation the optimal plane of reconstruction was found through sampling planes and determining the sharpest image. This eventually gave us the plane images of the source given in Figure 16 and 17.

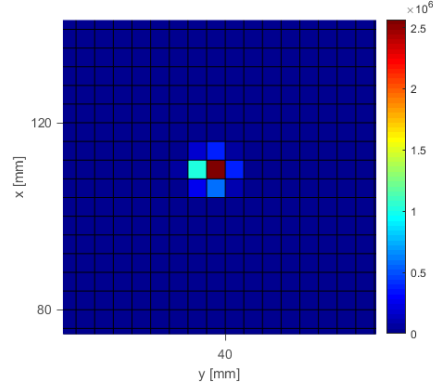


Figure 16: Measurement 2:
reconstruction of the source.

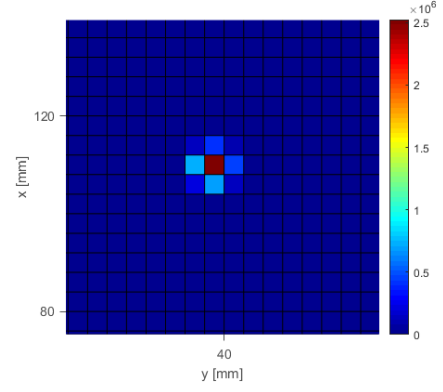


Figure 17: Measurement 3:
reconstruction of the source.

In the fourth and fifth measurement, the source was located in the midplane and moved around 50 mm in the negative x-direction in the fourth measurement and around 50 mm in the positive x direction in the fifth measurement. Unfortunately, the source was located on the edge of the Field Of View (FOV) in the fifth experiment, resulting in less data gathered. The field of view is the volume between the detectors that they can 'see'. As can be seen when comparing figure 18 and 19, the image reconstruction of the fifth measurement is partially cut off at the edge, resulting in a lower count rate. Also, it caused that the x-position of the source couldn't

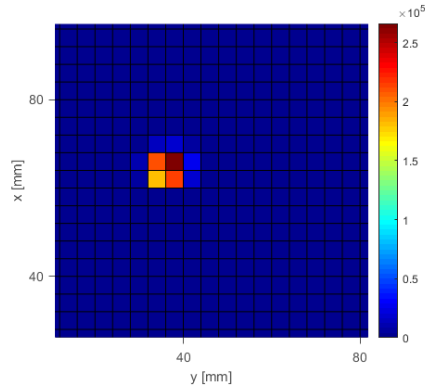


Figure 18: Measurement 4 midplane
image

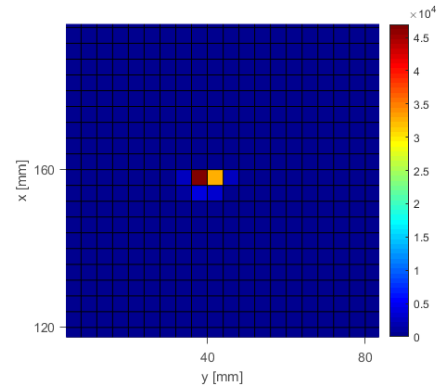


Figure 19: Measurement 5 midplane
image

be measured with precision. But using the y-axis, the spatial resolution could still be found. The fitted Gaussians and their parameters are given in Figure 20 and 21. It was found from comparing the spatial distribution of the fourth and fifth measurement with the first, that the displacement of the source was approximately 46.5 ± 0.1 mm in the fourth measurement and 46 ± 8 mm in the fifth measurement. The found spatial resolutions of all measurements are given in table 6.

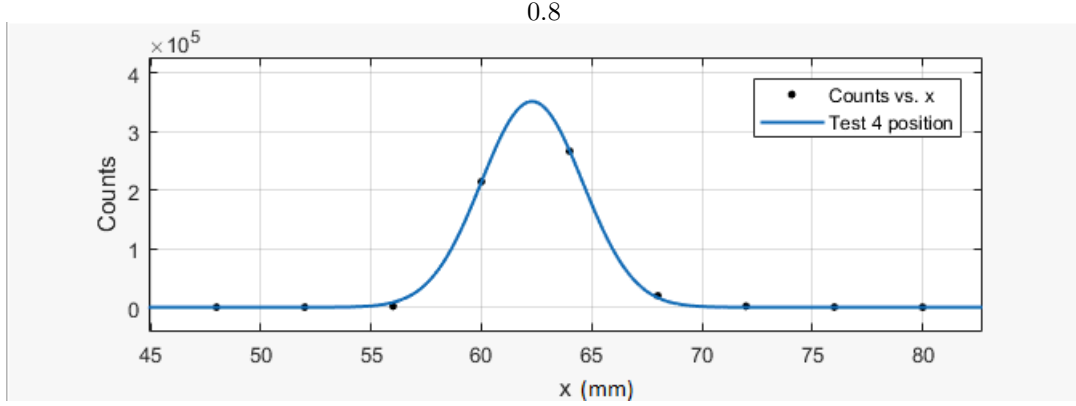


Figure 20: Measurement 4: Gaussian fitted position distribution with parameters: $a = (3.509 \pm 0.058) * 10^5$, $b = 60.3 \pm 0.02$, $c = 3.254 \pm 0.065$ and a R^2 of 0.9995.

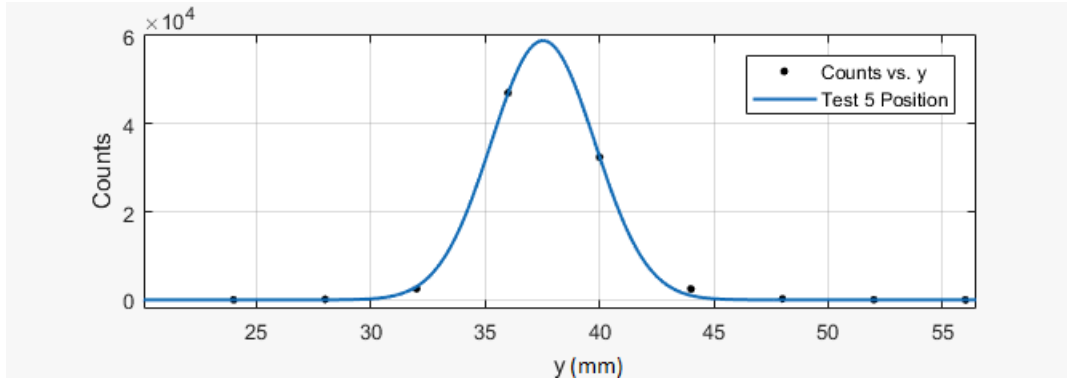


Figure 21: Measurement 5: Gaussian fitted position distribution with parameters: $a = (5.883 \pm 0.113) * 10^4$, $b = 37.53 \pm 0.03$, $c = 3.208 \pm 0.075$ and a R^2 of 0.9997 (note that this graph is plotted versus y instead of x).

4.3 processing time

For in vivo measurements, it is required for the observation to be processed in relatively short time. To give an estimation of the workload of these reconstructions table 7 was made with corresponding processing times for each of the measurements. The raw data obtained from the coincidence unit was first 'decoded' using a C++ program. The decoded data was subsequently analysed using Matlab. These two steps were performed on two different computers with different processors. The C++ program was run on a laptop with a *Intel(R) Core(TM) i5-3230M*

Table 6: Spatial resolution.

Measurement	Spatial resolution (ps)	x-position peak of the Gaussian (ps)	Averaged count rate (cps)
1	5.0 ± 0.1	106.8 ± 0.01	11201
2	5.1 ± 0.1	107.7 ± 0.01	9656
3	5.3 ± 0.1	107.7 ± 0.02	9361
4	5.4 ± 0.1	60.3 ± 0.02	1671
5	5.3 ± 0.2	153 ± 8	174

CPU @ 2.60GHz 2601 MHz 2 core('s), 4 logische processors(s) processor and the MATLAB program on a dekstop with a *Intel(R) Core(TM) 2 Duo CPU E8300 @2,83 GHz* processor.

Table 7: Processing Time for each measurement.

Measurement	Counts	C++ Time (s)	MATlab time (s)	Events processed per second
1	6720378	1.453	623.34	10756
2	5793790	1.333	497.82	11607
3	5616335	1.13	451.73	12401
4	1002436	1.227	87.77	11379
5	104603	1.185	12.24	7791

5 Discussion

5.1 Timing resolution

Table 4 displays the timing resolution for every measurement. If the timing resolution of every measurement for a single crystal is compared, it is found that an increase in count rate often gives rise to an increase in timing resolution. Also, there is a difference between the timing resolution of separate crystals. In the first measurement the crystals at the edge of the detector (ID 760 and 1342) have a lower timing resolution than the crystal in the middle (ID 979). This could possibly be accounted to the lower count rate, but to examine it further, more crystals throughout the detector were used to examine the timing resolution. The timing resolutions for a whole row of crystals of 1 block detector at a fixed height are given in Table 5 and are plotted in Figure 23. For illustration, the crystals used are given in Figure 22.

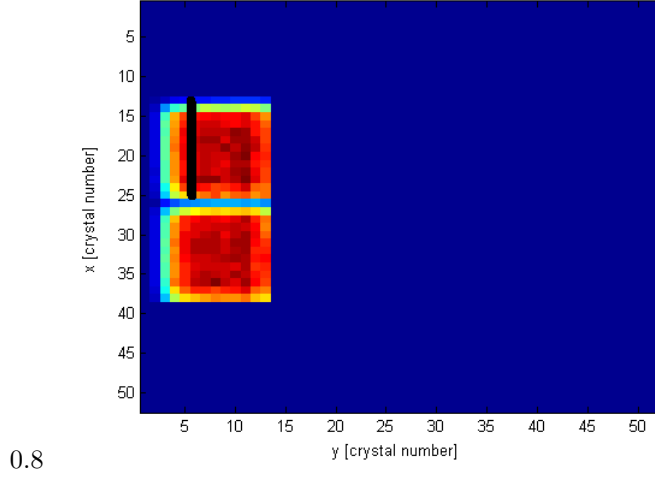


Figure 22: Measurement 1: The black bar resembles the 13 crystals examined

Uncertainties in timing resolution arise from the statistical nature of the signal (which is produced of the conversion of 511 keV photons into light and then electron in the detector) and from electronic noise in the detector and associated circuits. With the small amount of results that is acquired and the uncertainty of accuracy of the set-up, it is hard to conclude with certainty if this effect is true (and if so, what could be the cause). But from these results it seems like there could likely be a connection between timing resolution and position of the crystal in the detector. Further research may prove useful. This can be done with a more precise geometric set-up and more measurements, in where the source is moved inside the field of view, to see if the effect persists when the edge crystals receive a higher count rate. The only data sets usable in this report are measurement 1 and 4, the data of measurement 4 is given in Table 8. This data also suggest a slight relation between the improved timing resolution in the edge crystals but is too inaccurate to be conclusive.

Siemens stated in their manual the timing resolution to be typically around 540 ps. If the data from the 13 crystals of measurement 1 is averaged, a timing resolution of 532 ± 5 ps is obtained, in excellent agreement with the detector specifications.

Table 8: Measurement 4: Timing resolution for 5 adjacent crystal at fixed height.

Crystal ID	Timing Resolution (ps)	Averaged Count Rate (cps)
708	549 ± 5	37.2
760	536.33 ± 8	44.2
812	539.83 ± 4	39.4
864	545 ± 6	17.9
916	551 ± 10	4.4

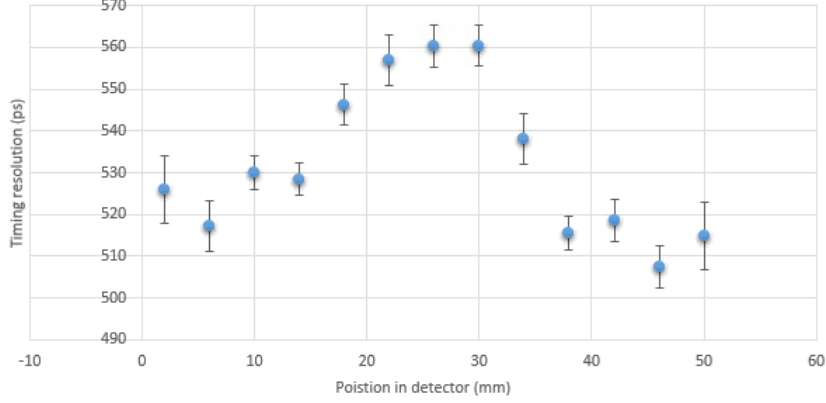


Figure 23: Measurement 1: Timing resolution vs x position in the scanner at a fixed height.

5.2 Spatial resolution

Table 6 gives the spatial resolutions for each of the five measurements. As expected, the ideal situation where the source is exactly in the middle (measurement 1), gives the best resolution: 5.0 ± 0.1 mm. In the Siemens manual (Figure 3), the spatial resolution is said to be 5.5 mm. When the source is repositioned closer to one of the two detectors, its spatial resolution is expected to get worse. Geometrically, when the source is moved 7.62 cm closer to scanner panel A, the amount of photons that will pass through detector panel A increases from 3.01% to 5.09%. For B it decreases from 3.01% to 2.00%. Formula 3 tells us the total amount of random coincidences thus increases by 12.3%. While the amount of true coincidences will decrease with 34%, because the effective area (limiting factor detector panel B) decreases, to 66% of its area in the first measurement. It is expected for the spatial resolution to increase when the source is moved towards one of the detector panels, that is also seen in table 6. The spatial resolution also worsened in the fourth and fifth measurement. Originally, because the same distance between the scanners and the source is kept the spatial resolution was expected to be equal to that of the first measurement. It is only a small difference which almost be completely accounted for by the error margin. It is suspected that the small error that arose is probably due to the geometrical inefficiency of the set up. One of the possibilities is that one of the block detectors had an slight angle compared to the others. In a measurement (4+5) with only two detectors that measure coincidences the resulting error is larger than when 4 detectors are used. Still, the obtained spatial resolutions are all in close approximation to each other and the given value by Siemens of 5.5 mm.

5.3 Recommendation for further Investigation

To further the examination of these detector, one could of course perform more of the same measurements under better geometrically accuracy and try to find better resolutions. But for now, it is believed that the resolutions found in this report are accurate and sufficient. To investigate the relation between time difference and position inside the scanner mentioned in section 5.1 one could perform more measurements where the source is moved inside the midplane.

6 Conclusion

Five measurements were performed to examine the spatial and timing resolution of a Siemens TOF-PET detector based on the Biograph mCT Flow. A 8.1×10^6 Bq source was used with a detector panel separation of 43 cm. From the acquired data, the midplane image was reconstructed and with the use of Gaussian fits in the spatial and time distribution, the resolutions were determined. The measurements yielded a spatial resolution of 5.0 ± 0.1 mm and a timing resolution of 532 ± 5 ps. The first measurement served the purpose of verifying the resolutions while the other four were used to examine the effect of a change in source position. The speed of the necessary processing for a *Intel(R) Core(TM) 2 Duo CPU E8300 @2,83 GHz* processor is examined and averaged to around 1.1×10^4 events per second. This knowledge is useful when future investigations are performed with these detectors.

References

- [1] Assmann W, Kellnberger S, Reinhardt S, Lehrack S, Edlich A, Thirolf P G, Moser M, Dollinger G, Omar M, Ntziachristos V, Parodi K (2015) 'Sonoacoustic characterization of the proton Bragg peak with submillimeter accuracy' *Med. Phys.* 42 567–74
- [2] Buitenhuis H J T, Diblen F, Brzezinski K W, Brandenburg S, Dendooven P, (2017) 'Beam-on imaging of short-lived positron emitters during proton therapy' *Phys. Med. Biol.* 62 (2017) 4654–4672
- [3] Cal-González et al, (2013) 'Positron range estimations with PeneloPET' *Phys. Med. Biol.* 58 5127
- [4] Cherry Simon R. , Sorenson James A. , Phelps Michael E. , (2012) 'Physics in Nuclear Medicine'
- [5] Dendooven P, Buitenhuis H J T, Diblen F, Heeres P N, Biegun A K, Fiedler F, van Goethem M-J, van der Graaf E R, Brandenburg S, (2015) 'Short-lived positron emitters in beam-on PET imaging during proton therapy' *Phys. Med. Biol.* 60 (2015) 8923–8947
- [6] Gopal B Saha, (2010) 'Basics of PET imaging, Physics, Chemistry, and Regulations, Second Edition'
- [7] Jones K C, Nie W, Chu J C H, Turian J V, Kassaei A, Sehgal C M, Avery S, (2018) 'Acoustic-based proton range verification in heterogeneous tissue: simulation studies' *Phys. Med. Biol.* 63 025018
- [8] Krimmer J et al, (2018) 'Prompt-gamma monitoring in hadrontherapy: A review' *Nucl. Instrum. Meth. Phys. Res. A* 878, 58-73

- [9] Lang S, Riesterer O, (2013) 'Modern Techniques in Radiation Oncology' *Swiss Physical Society* <https://www.sps.ch/en/articles/progresses/modern-techniques-in-radiation-oncology-36/>
- [10] Nie W et al, (2018) 'Proton range verification in homogeneous materials through acoustic measurements' *Phys. Med. Biol.* 63 025036
- [11] NNDC 2015 N-12 http://www.nndc.bnl.gov/nudat2/dec_searchi.jsp
- [12] Peter V E, Dale B L, David T W, Micheal M N, (2004) 'Positron Emission Tomography, Basic Science and Clinical Practice'
- [13] PTCOG Facilities in operation <https://ptcog.ch/index.php/facilities-in-operation>
- [14] Richter et al (2016) 'First clinical application of a prompt gamma based in vivo proton range verification system' *Volume 118, Issue 2, February 2016, Pages 232-237*
- [15] Rizzi M, D'Aloia M, and Castagnolo B, (2010) 'Semiconductor Detectors and Principles of Radiation-matter Interaction', *Journal of Applied Sciences*, 10: 3141-3155.
- [16] Siemens, (2009) Inside Biograph TruePoint PET•CT
- [17] Siemens, (2013) Biograph mCT Flow Product Specification Sheet www.Siemens.com/learn-about-mCT-Flow
- [18] Smeets J et al, (2012) 'Prompt gamma imaging with a slit camera for real-time range control in proton therapy' *therapy Phys. Med. Biol.* 57 3371-405
- [19] Tobias C A et al, (1958) 'Pituitary Irradiation with High-Energy Proton Beams A Preliminary Report' *Cancer Res February 1 1958 (18) (2) 121-134*
- [20] Vandenberghe S, Mikhaylova E, D'Hoe E, Karp S J, 2016, 'Recent developments in time-of-flight PET', *EJNMMI Physics* 3:3
- [21] Verburg J M, Seco J, (2014) 'Proton range verification through prompt gamma-ray spectroscopy' *Phys. Med. Biol.* 59 7089
- [22] Wikipedia Composition of the human body https://en.wikipedia.org/wiki/Composition_of_the_human_body#Tissues
- [23] Wilson R R, (1946) 'Radiological Use of Fast Protons' *Radiology* 1946 47:5, 487-491
- [24] Yao R, Ma T, Shao Y, (2008) 'Lutetium oxyorthosilicate (LSO) intrinsic activity correction and minimal detectable target activity study for SPECT imaging with a LSO-based animal PET scanner' *Phys. Med. Biol.* 53 4399
- [25] 'SPECT - Attenuation Scatter and its Resolution' <http://www.people.vcu.edu/~mhcrosthwait/clrs322/attenuationandscatter.html#moreonscatter>